

Surface Processing and Discharge-Conditioning of High Voltage Electrodes for the Ra EDM Experiment

Roy A. Ready^a, Gordon Arrowsmith-Kron^a, Kevin G. Bailey^b, Dominic Battaglia^a, Michael Bishop^b, Daniel Coulter^a, Matthew R. Dietrich^b, Ruoyu Fang^a, Brian Hanley^a, Jake Huneau^a, Sean Kennedy^a, Peyton Lalain^a, Benjamin Loseth^a, Kellen McGee^a, Peter Mueller^b, Thomas P. O'Connor^b, Jordan O'Kronley^a, Adam Powers^a, Tenzin Rabga^a, Andrew Sanchez^a, Eli Schalk^a, Dale Waldo^a, Jacob Wescott^a, Jaideep T. Singh^a

^aNational Superconducting Cyclotron Laboratory and Department of Physics and Astronomy, Michigan State University, East Lansing, Michigan 48824, USA

^bPhysics Division, Argonne National Laboratory, Argonne, Illinois 60439, USA

Abstract

The Ra EDM experiment uses a pair of high voltage electrodes to search for the atomic electric dipole moment of ^{225}Ra . We use identical, plane-parallel electrodes with a primary high gradient surface of 200 mm^2 to generate reversible DC electric fields. Our statistical sensitivity is linearly proportional to the electric field strength in the electrode gap. We adapted surface decontamination and processing techniques from accelerator physics literature to chemical polish and clean a suite of newly fabricated large-grain niobium and grade-2 titanium electrodes. Three pairs of niobium electrodes and one pair of titanium electrodes were discharge-conditioned with a custom high voltage test station at electric field strengths as high as $+52.5\text{ kV/mm}$ and -51.5 kV/mm over electrode gap sizes ranging from 0.4 mm to 2.5 mm . One pair of large-grain niobium electrodes was discharge-conditioned and validated to operate at $\pm 20\text{ kV/mm}$ with steady-state leakage current $\leq 25\text{ pA}$ (1σ) and a polarity-averaged 98 ± 19 discharges per hour. These electrodes were installed in the Ra EDM experimental apparatus, replacing a copper electrode pair, and were revalidated to $\pm 20\text{ kV/mm}$. The niobium electrodes perform at an electric field strength 3.1 times larger than the legacy copper electrodes and are ultimately limited by the maximum output of our 30 kV bipolar power supply.

Keywords: high voltage electrode conditioning, leakage current, large-grain niobium, radium-225, atomic electric dipole moment, magnetic Johnson noise

1. Ra EDM Motivation and Requirements

1.1. Motivation

Violation of combined charge conjugation (C) and parity (P) symmetry, or CP , is a necessary ingredient of the observed dominance of matter over antimatter, or baryon asymmetry of the universe (BAU). CP violation is encoded in the Standard Model (SM) by a complex phase term in the Cabibbo-Kobayashi-Maskawa (CKM) quark mixing matrix [1]. The SM critically underestimates the BAU, suggesting that new sources of CP violation have yet to be discovered [2].

Permanent electric dipole moments (EDMs) violate time-reversal (T) and P symmetry. Assuming CPT conservation, EDMs also violate CP . Neutron, electron, molecular, and atomic EDM experiments have been carried out over the last seven decades in an effort to measure a nonzero EDM magnitude. While nonzero EDMs remain out of reach for now, the precision of EDM measurements continues to improve. Observing a nonzero EDM near sen-

sitivities of today's leading experiments would provide a clean signature of Beyond the Standard Model physics [1].

The atomic EDM of ^{225}Ra (spin $I = 1/2$) is enhanced by the octupole deformation ("pear shape") of its nucleus. Radium-225 has a 55 keV parity doublet ground state structure, compared to approximately 1 MeV in spherically symmetric nuclei [3]. This enhances the observable component of the EDM, characterized by the nuclear Schiff moment. The Schiff moment of ^{225}Ra is predicted to be up to three orders of magnitude larger than that of diamagnetic atoms with spherically symmetric nuclei [4, 5, 6, 7].

The Ra EDM experiment (Argonne National Lab, Michigan State University) measures the spin precession frequency of ^{225}Ra in a controlled, uniform magnetic and electric field between two high voltage electrodes in an optical dipole trap (ODT). EDM measurements are performed at Argonne National Lab (ANL), while offline upgrades such as the high voltage development discussed in this report are carried out at Michigan State University (MSU). In the proof of principle measurement, the EDM 2σ upper limit was measured to $5.0 \times 10^{-22}\text{ e cm}$ [8]. This was reduced to $1.4 \times 10^{-23}\text{ e cm}$ in the subsequent run [9]. Hereafter we will refer to these as the 'first generation'

Email address: roy.a.ready@gmail.com (Roy A. Ready)

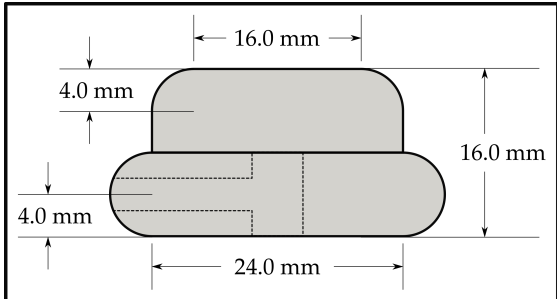


Figure 1: Cross-sectional electrode schematic. Surfaces have a flatness tolerance of $25.4 \mu\text{m}$ and a parallelism of $50.8 \mu\text{m}$. The top surface is polished to an average roughness of $0.127 \mu\text{m}$. The base is mounted by a 10-32 tapped hole.

measurements.

The shot noise-limited EDM standard error σ_{EDM} (e cm) is given by:

$$\sigma_{\text{EDM}} = \frac{\hbar}{2E\sqrt{\epsilon NT\tau}}, \quad (1)$$

where

- E (V/cm) is the external electric field,
- \hbar (eV s) is the reduced Planck constant,
- ϵ (unitless) is the atom detection efficiency,
- N (unitless) is the number of atoms per sample,
- T (s) is the total measurement time, and
- τ (s) is the measurement time per cycle.

As seen in Equation 1, the statistical sensitivity of the EDM measurement scales linearly with the electric field strength. The Ra EDM experiment will be significantly improved with targeted upgrades to the experimental apparatus over the next several ‘second generation’ measurements. In particular, we will use a new atom detection method to increase ϵ and new electrodes to increase E . We will surpass the 10^{-25} e cm sensitivity level during this phase and the ^{225}Ra EDM limit will constrain hadronic CP -violating parameters alongside other EDM experiments [10].

1.2. High voltage experimental requirements

The EDM couples to an external electric field analogously to the coupling of the atomic magnetic dipole moment to an external magnetic field. The Hamiltonian of an atom in the presence of a perfectly uniform electric and magnetic field is given by the following:

$$\mathcal{H} = -\mu \left(\frac{\vec{S} \cdot \vec{B}}{S} \right) - d \left(\frac{\vec{S} \cdot \vec{E}}{S} \right), \quad (2)$$

where

- $\mu = -2.3 \times 10^{-8}$ eV/T is the atomic magnetic dipole moment of ^{225}Ra [11],
- \vec{S} is the total atomic angular momentum,
- \vec{B} (T) is the applied magnetic field,

Table 1: Ra EDM systematic requirements at the 10^{-26} e cm sensitivity level. Detailed descriptions of evaluations of θ_E , $|\Delta E|/E$, and \bar{I} can be found in our previous work [9]. ΔB is determined by Equation 5. We describe our calculation of the Johnson noise limit in Appendix A.

description	systematic limit	
\vec{E} , \vec{B} alignment	θ_E	≤ 2 mrad
polarity imbalance	$\frac{ \Delta E }{E}$	$\leq 0.7\%$
electrode magnetic impurity	ΔB	≤ 100 fT ^a
steady-state leakage current	\bar{I}	≤ 100 pA ^a
magnetic Johnson noise	$\sqrt{\frac{dB_n^2}{d\nu}}$	$\leq 15 \frac{\text{pT}^a}{\sqrt{\text{Hz}}}$

^a per measurement cycle

d (e cm) is the atomic EDM, and

\vec{E} (V/cm) is the applied electric field.

The ^{225}Ra atoms will precess with frequency ω_+ (ω_-) when \vec{E} is parallel (antiparallel) to \vec{B} :

$$\omega_{\pm} = \frac{2}{\hbar}(\mu B \pm dE) \text{ rad/s} \quad (3)$$

In the most recent Ra EDM experiment we applied a $2.6 \mu\text{T}$ magnetic field and measured a spin precession frequency of 181.1 ± 1.6 rad/s [9].

We use a pair of identical plane-parallel electrodes to produce a stable, uniform, and symmetric electric field. The spin precession of the atoms is measured in three configurations: with the electric field parallel to the magnetic field, with the electric field antiparallel to the magnetic field, and with no applied electric field. The ‘field-off’ setting is used to control for a systematic effect generated by an imperfect reversal of the electric field. We measure the accumulated spin precession phase for each field configuration. The extracted EDM is related to the accumulated phase difference between the parallel and antiparallel configurations by Equation 4:

$$d = \frac{\hbar \Delta \phi}{4E\tau}, \quad (4)$$

where $\Delta \phi$ (rad) is the difference in accumulated phase between the two ‘field-on’ configurations. With a perfectly uniform and static magnetic field under all configurations, the phase difference between the parallel and antiparallel field configurations is purely due to the EDM interaction with the electric field. A higher electric field strength will generate a larger accumulated phase and improve EDM sensitivity.

In one measurement cycle, one electrode is charged to $\leq +30$ kV (positive polarity) while the other is grounded. The atom trap lifetime is currently about twenty seconds. We expect to increase the trap lifetime to one hundred seconds [12] as improvements are made to the ODT. The

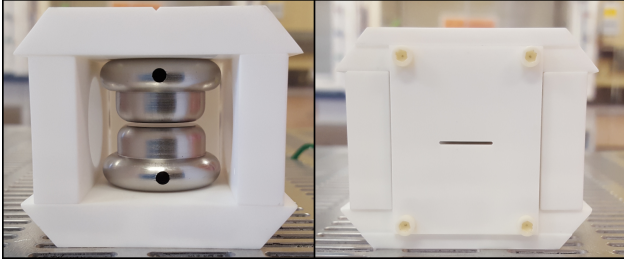


Figure 2: Left: assembly of the niobium pair Nb_{56} at 1 mm gap in Macor holder. Right: a slit centered on the gap shields the electrode surfaces from heating by the atom-trapping and excitation lasers.

charged electrode is then ramped to zero voltage and remains grounded for a period of 60 s while a new sample of atoms is prepared. The next cycle begins and the electrode is charged to the same voltage magnitude at negative polarity. We repeat this process until the atomic oven is depleted after approximately two weeks.

Now we will discuss EDM measurement systematics related to the high voltage system. Our requirements for each systematic are given in Table 1.

The electric field between the electrodes must be symmetric, uniform, and reversible to minimize systematic effects. The alignment between \vec{E} and \vec{B} is fixed after mounting the electrodes to the Macor holder, as shown in Figure 2. In the experimental apparatus, the holder and electrodes rest within a borosilicate glass tube. We will use vector fluxgates with a system of autocollimators to optically determine the field uniformity and alignment for the second generation EDM measurements [13]. The field reversibility is measured with a calibrated high voltage divider (Ross Engineering V30-8.3-A).

Magnetic field fluctuations caused by current in the electrodes, or magnetic Johnson noise, limits the choice of electrode materials and geometries that are suitable for an EDM measurement. The magnetic field scales as $\rho^{-1/2}$, where ρ ($\Omega \text{ m}$) is the resistivity. For two niobium electrodes separated by 1 mm with the geometry shown in Figure 1, we estimate the magnetic Johnson noise per sample to be $2.48 \text{ pT}/\sqrt{\text{Hz}}$. For an EDM measurement lasting $T = 15$ days with an atom spin precession time of $\tau = 100$ s and an electric field of 30 kV/mm (see Equation 1), magnetic Johnson noise will only become significant at the $10^{-26} e \text{ cm}$ level. A detailed description of magnetic Johnson noise calculations is given in Appendix A.

We consider an additional systematic in which the magnetization of a fraction of the impurities in the electrodes depends on the polarity of the charging current. A sufficiently high concentration of paramagnetic impurities near an electrode primary surface could perturb the magnetic field in the radium cloud region. This would generate an atomic precession frequency mimicking an EDM signal, which can be expressed as a “false” EDM $d_{\Delta B}$:

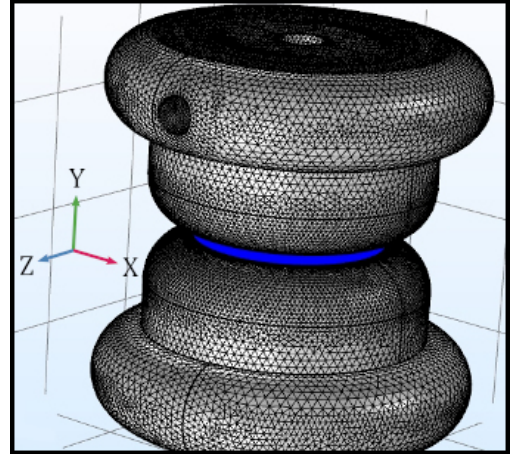


Figure 3: A COMSOL meshed model of the electrodes with the region of interest shaded blue. The origin is 0.5 mm below the top electrode surface, centered on the top electrode. When the bottom electrode is aligned with the top electrode, the origin is exactly in the center of the electrode gap.

$$d_{\Delta B} = \frac{\mu \Delta B}{E}, \quad (5)$$

where ΔB is the local magnetic field change from magnetic impurities in the electrodes as the electric field is reversed.

For a local magnetic field change $\Delta B \approx 100 \text{ fT}$ per 30 kV/mm field reversal, this systematic will only become significant at the $10^{-26} e \text{ cm}$ level. Measuring a magnetic field strength of this magnitude will require more sensitive techniques than the low-noise fluxgate magnetometers (Bartington Mag-03MSL70) we currently use.

To minimize systematic effects due to magnetic impurities, we use high-grade electrode materials and surface processing techniques that remove contaminants. Tables 2 and 3 list the material properties and processing techniques that we use. We will discuss electrode material selection and surface processing in detail in Section 2.

1.3. Electric field and laser interactions

A radium sample is trapped in the electrode gap by an ODT for each EDM measurement cycle. We induce coherent atomic spin precession in the controlled magnetic and electric field with a polarizing laser pulse. The spin precession frequency is measured by firing a subsequent ‘detection’ laser pulse and imaging the atom cloud photon absorption fraction after a variable delay time δ (ms).

We considered two methods for the sequencing of the polarization pulse, detection pulse, and the electric field ramping. In the first method, the polarizing laser pulse is fired after the electric field ramps on and the detection pulse is fired before the field ramps off. This shifts the ^{225}Ra ground state due to an interaction between the ODT polarization and the DC electric field. In the second method, the polarizing laser pulse is fired before ramping the field on and after ramping the field off. This pulse sequence avoids potential mixing of the excited state hyper-

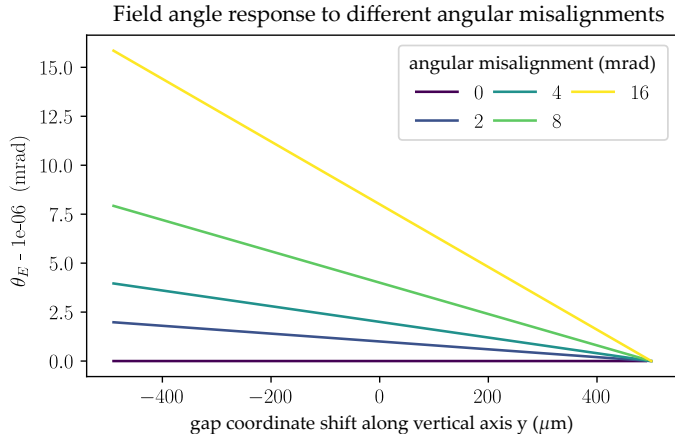


Figure 4: θ_E as a function of the vertical distance y when the electrodes are axially aligned for a range of tilts. At $y = 0$, θ_E is evaluated 0.5 mm below and centered on the top electrode.

fine levels and suppresses atomic polarization from ODT and electric field interactions.

The Ra EDM experiment uses the second method to measure the spin precession frequency. We also consider spin precession perturbations caused by transient magnetic fields that are generated during electrode charging. This effect is suppressed if the ramping on and ramping off pulse shapes are symmetric. Even with zero charging field cancellation, this systematic will only become significant at the 10^{-27} e cm level [9].

1.4. Electrode geometry

Two identical electrodes make up the Ra EDM electrode pair. The primary surface, seen as the top surface in Figure 1, is flat and 16 mm in diameter. The rounded edges have 4 mm circular radial curvatures. We use plane-parallel electrodes (see Figure 2) so that the reversible field is uniform and symmetric as the electrodes alternate roles as cathode and anode every EDM measurement cycle.

The Ra EDM experiment requires an applied electric field that is symmetric, uniform, and reversible in the center of the electrode gap where the spin precession frequency of the 50 μm diameter radium cloud is measured. Our electrode geometry reliably meets these requirements at field strengths of 12–30 kV/mm. In Section 1.5 we will use finite element modeling to show that the electric field generated by our electrodes matches that of the ideal infinite-plane capacitor in the atom cloud region.

Systematic effects arising from asymmetric field reversal must continue to be reduced as EDM statistical sensitivity improves. In the current measurement scheme, one electrode is permanently grounded and the other electrode is charged by a bipolar power supply. We will design a more symmetric apparatus that allows us to alternate the charged and grounded electrodes using high voltage switches and a unipolar 50 kV power supply in the next phase of high voltage development. In addition, we will optimize the electrode geometry to reduce field edge effects

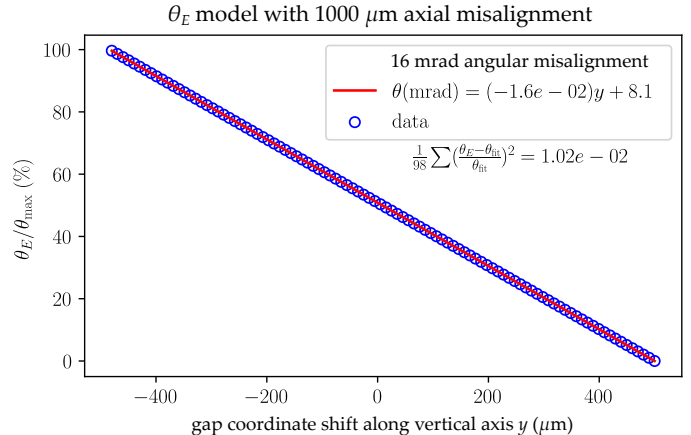


Figure 5: A linear fit to the simulated electric field polar angle with the bottom electrode tilted 16 mrad and shifted 1 mm. At $y = 0$, θ_E is evaluated 0.5 mm below and centered on the top electrode.

using the computational modeling described in Section 1.5.

1.5. Field angle response to electrode misalignment

One systematic that creates a “false” EDM-like signal scales with the sine of the angle between the electric field and the controlled uniform magnetic field we use for measuring the spin precession frequency of the radium atoms. We modeled the high voltage electrodes in the finite element analysis software COMSOL Multiphysics (version 5.3) to study the electrostatic behavior as the alignment is varied from perfectly parallel, axially-centered electrodes. In the model, the electrodes are surrounded by a perfect vacuum. The electrode gap size is fixed at 1 mm and the top electrode is charged to -30 kV for a nominal electric field of $E_0 = 30$ kV/mm.

Our simulations use the **Extremely Fine** settings with **Size Expression** increased to 4×10^{-4} in the gap region and **Resolution** increased to 200 along the upper curved electrode surface. We reduced the minimum mesh element size to 20 μm , where we found that the electric field dependence on the mesh size converges to negligibly small fluctuations.

The coordinate system of the electrode pair electrostatic model is shown in Figure 3, with the origin defined as the midpoint between the two electrodes along their vertical axis of the top electrode. We find that the vertical field strength E_y changes by less than 6 ppb per 100 μm when the electrodes are perfectly aligned. The horizontal field magnitude $E_{\perp} = \sqrt{E_x^2 + E_z^2}$ changes by less than 5 ppb per 100 μm with respect to E_0 within 0.5 mm of the origin. In practice, we align our electrodes to better than 4 mrad in the high voltage test stand described in Section 3.1.

We investigated the effect of misalignments between the electrodes on the electric field angle, defined as $\theta_E = \arctan(E_y/E_{\perp})$. There are two types of misalignments we consider. Angular misalignments, or tilts, are introduced by rotating the bottom electrode about the z axis in the range 0–16 mrad. Axial misalignments, or

Table 2: Bulk material properties of electrodes.

material	Z	ϕ (eV)	strong magnetic impurity (%) ^a	density (kg/m ³)	resistivity ($\mu\Omega$ cm) ^b	hardness (kgf/mm ²)	outgas rate (Torr nL s ⁻¹ cm ⁻²)
niobium ^c	41	4.3	2.7×10^{-2}	8570	15.2	134.6	30
copper ^d	29	4.65	2.5×10^{-7}	8960	1.543	35.0	16.3
titanium ^e	22	4.33	5.5×10^{-1}	4506	39	99.0	184
stainless steel ^f	-	4.34	$8.1 \times 10^{+1}$	8000	69.0	176	42.8
molybdenum ^g	42	4.6	1.4×10^{-2}	10200	4.85	156.0	36.7
			References				
		[14, 15]	[16]	[16, 17]	[18, 19]	[20, 17]	[21, 22]

^a We define “strong magnetic impurities” as $\chi_m/(10^{-6} \text{ cm}^3 \text{ mol}^{-1}) > +1000$, where χ_m is the molar susceptibility. $\chi_m(\text{Nb}) = +208$.

^b Resistivity measured at 273 K.

^c Hardness for at 473 K. Outgas rate estimated from the correlation between Cu, SS, and Nb desorption.

^d Hardness of single crystal (III) at 293 K. Outgas rate for unbaked OF high-conductivity after ten hours.

^e Hardness of iodide-annealed, 99.99% purity at 293 K. Outgas rate for unbaked OF high-conductivity after ten hours.

^f Hardness of designation type 304. Outgas rate for unbaked, electropolished NS22S after ten hours.

^g Hardness measured at 293 K.

shifts, translates the bottom electrode along the x axis and offsets the electrode centers. Shifts of up to 1 mm displacements are considered in this work. When the tilt and shift are zero, the electrodes are perfectly aligned and $\theta_E = 0$ near the center of the gap, corresponding to a uniform vertical field.

The electric field angle scales linearly with the angular misalignments, as shown in Figure 4. We modeled the change in θ_E as a linear function of the position in both the xy plane (Figure 5) and the xz plane. The linear model reproduces the change in the electric field angle to an accuracy of better than 1 μrad in both planes up to 1 mm from the center of the gap, even for large angular and axial misalignments.

The vertical field strength is reduced minutely even for the severe 16 mrad tilt and 1 mm shift we have modeled in Figure 5. We find the vertical field strength fractional change $\Delta E_y/E_0 \approx 230$ ppm per 500 μm from the origin. The electrode shift effectively changes the gap size near the origin, causing a constant offset in the vertical field strength. For the case of a 16 mrad angular misalignment and 1 mm axial misalignment, the offset in E_y is 1.6%.

We show in Figure 5 that the field angle is described by a linear function of the vertical (y) coordinate. Initially vertical ($\theta_E = 0$) at the top surface of the electrode, the field angle changes by 1% of the electrode tilt per 10 μm along the y axis. The field angle is 8 mrad at the midplane halfway between the electrodes and 16 mrad at the surface of the bottom electrode. If we scan horizontally in the midplane along the x axis towards the electrode edge, the polar angle changes by 0.03% per 10 μm .

In the more realistic case of a 2 mrad tilt, we find that θ_E changes by 0.2 μrad per 100 μm in the vertical plane and 0.02 μrad per 100 μm in the midplane. EDM systematic effects arising from field angle changes of this magnitude are far below our current statistical sensitivity.

1.6. High voltage upgrade strategy and results

We define discharge-conditioning as the process of applying iteratively higher voltages to the electrodes to suppress steady-state leakage current and discharge rates between them. Leakage current refers to any current flowing between the electrodes detected by a picoammeter in series with one of the electrodes, as shown in Figure 6. We differentiate our method from the standard “current-conditioning” method [23] because we characterize electrode performance by counting discrete discharges over time and we use a periodic voltage waveform. In this paper we will interchangeably use the shorthand term “conditioning” when referring to discharge-conditioning.

In the absence of surface particulate contamination, electrode discharges are caused by charge buildup on microprotrusions on the electrode surfaces [24], which we will refer to as charge emitters. We process and handle our electrodes in Class 100 or better environments to minimize particulate contamination. The height of charge emitters have been measured on the order of 1 μm in buffer chemical-polished large-grain niobium electrodes prepared similarly to our electrodes [25]. If the charge emitter is near the edge of the electrode, we expect the higher gradients will increase the likelihood of a discharge.

Controlled discharges electrically polish away, or ablate charge emitters over time, allowing the electrodes to perform reliably at higher voltages [23]. As shown in Section 3, it may take tens to more than one hundred hours of discharge-conditioning to suppress charge emitters. We expect the required conditioning duration may take longer if the surface is insufficiently polished or contaminated. Bulk properties, such as the work function, resistivity, or hardness of the electrode may also play a role in the conditioning time. These bulk properties are listed for a selection of commonly used electrode materials in Table 2.

Four pairs of niobium electrodes and two pairs of titanium electrodes were surface processed as described in

Table 3: Ra EDM electrode inventory. The large-grain (LG) niobium electrodes have a residual resistance ratio (RRR) > 250 . OF = oxygen free. G2 = grade-2. Simichrome polish by hand. Diamond paste polish (DPP) by hand. LPR = low pressure rinse. HPR = high pressure rinse. HF = hydrofluoric chemical polish. EP = electropolish. BCP= buffered chemical polish. SiC = silicon carbide machine polish. CSS = colloidal silica suspension machine polish. VB = 420–450 °C vacuum outgas bake. WB = 150–160 °C water bake. USR = ultrasonic rinse after detergent bath.

batch	material	pair	surface processing recipe					
1	OF copper	Cu ₁₂ ^a	Simichrome	→ EP	→ USR	→ WB		
2	LG niobium	Nb ₁₄	SiC	→ BCP	→ DPP	→ CSS	→ USR	→ VB ...
			... LPR	→ HPR				
2	LG niobium	Nb ₂₃	SiC	→ BCP	→ USR	→ VB	→ HPR	→ resurface ...
			... BCP	→ HPR				
2	G2 titanium	Ti ₂₄	SiC	→ HF	→ USR	→ VB	→ HPR	
2	G2 titanium	Ti ₁₃	SiC	→ HF	→ EP	→ USR	→ VB	→ HPR
3	LG niobium	Nb ₅₆ ^b	SiC	→ BCP	→ USR	→ HPR	→ WB	
3	LG niobium	Nb ₇₈	SiC	→ BCP	→ USR	→ HPR		

^a Legacy electrodes used for first two measurements [8, 9].

^b Second generation electrodes described in this work and currently installed in the Ra EDM apparatus.

Table 3. After high-pressure rinsing they are preserved in clean room environments of Class 100 (ISO 5) or better. We conditioned pairs of electrodes in a custom, Class 100-rated high voltage test station at MSU by applying DC voltages as high as ± 30 kV at gap sizes in the range 0.4–2.5 mm. Maximum fields of $+52.5$ kV/mm and -51.5 kV/mm were tested and are discussed in Section 3.7.

One pair of large-grain niobium electrodes was validated to operate reliably at 20 kV/mm at MSU. The electrodes were mounted in a stainless steel container and sealed in tubing backfilled with particle-filtered, dry nitrogen and were transported to ANL. We then constructed and validated a Class 100 clean room that covered the electrode entry point to the Ra EDM experimental apparatus. The electrodes were removed from their packaging and installed in the apparatus in May 2018, where they were revalidated to 20 kV/mm.

In Section 2 we will describe our past and present considerations in electrode material and surface processing. We start by describing the preparation of the previous electrode pair used for the first generation EDM measurements in Section 2.1. Material selection, surface processing, and electrode decontamination for the new electrodes tested in this work are detailed in Sections 2.2 and 2.3. We will present our method of benchmarking the performance of the electrodes in Section 3. Finally, we will summarize our findings and outline a roadmap for future Ra EDM high voltage development in Section 4.

2. Electrode Properties and Preparation

2.1. Legacy electrode preparation

The first generation EDM measurements used a pair of electropolished oxygen-free copper electrodes [8, 9]. Their geometry is identical to the new electrodes discussed in this

work (Figure 1). Surface processing of these electrodes, labeled as Cu₁₂, is detailed in Table 3.

The legacy electrodes were conditioned at ANL with a unipolar -30 kV power supply (Glassman PS/WH-30N15-LR) in a Macor holder at a 2 mm gap size in 2008 [26]. The electric field was reversed by turning the system off and manually switching the power supply terminations at the high voltage feedthroughs. Voltage was increased from 1–20 kV in 1 kV steps while monitoring the steady-state leakage current. Conditioning was declared complete if the electrodes could hold 20 kV with a steady-state leakage current of < 100 pA for ten hours.

Four pairs of electrodes total were tested in this manner, including two pairs of titanium electrodes and one pair of copper electrodes without electropolishing. The legacy titanium electrodes all exhibited leakage current higher than 100 pA at 20 kV. Flooding the test chamber with argon gas and plasma discharge-conditioning the titanium electrodes was attempted without an observable benefit. Both copper electrode pairs were conditioned, with the electropolished (EP) electrodes taking significantly less time.

The legacy electrode pair Cu₁₂ was mounted in a Macor holder at a 2.3 mm gap size and installed in the Ra EDM experimental apparatus [27]. The pair was retested at 20 kV / 2.3 mm = 8.7 kV/mm but exceeded the 100 pA limit. This was remedied by reducing the electric field by 25% to 6.5 kV/mm for the EDM measurement. We suspect that the primary surface of one or both of these legacy electrodes was contaminated during installation. This was a motivating factor in the development of the decontamination techniques for the new electrodes discussed in subsequent sections.

2.2. Consideration of materials for new electrodes

We selected large-grain niobium and grade-2 titanium for testing after reviewing accelerator physics literature. The bulk properties of these metals and other commonly

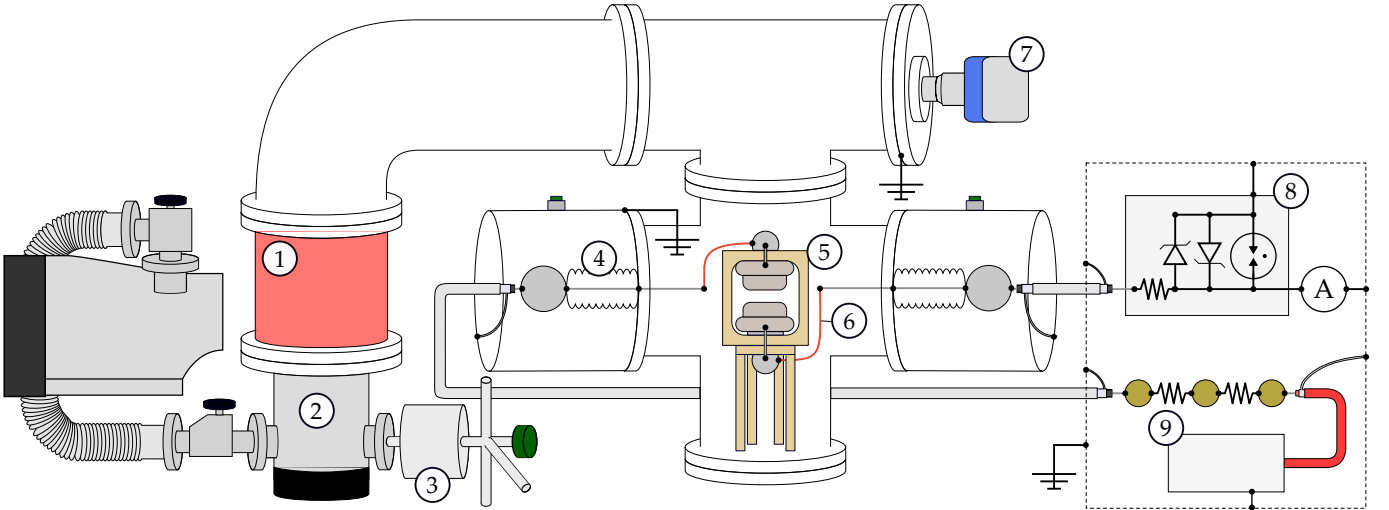


Figure 6: MSU HV test apparatus. ① 9699334 Agilent Turbo-V vibration damper ② Pfeiffer HiPace 80 turbomolecular pump with foreline Edwards nXDS10i A736-01-983 dry scroll rough pump and two valves ③ Matheson 6190 Series 0.01 micron membrane filter and purge port ④ Ceramtec 30 kV 16729-03-CF HV feedthroughs ⑤ 0.312 in.² electrodes in PEEK holder (resistivity 10^{16} M Ω cm) ⑥ 20 AWG Kapton-insulated, gold-plated copper wire ⑦ MKS 392502-2-YG-T all-range conductron/ion gauge ⑧ Shielded protection circuit: Littelfuse SA5.0A transient voltage suppressor, EPCOS EX-75X gas discharge tube, Ohmite 90J100E 100 Ω resistor in series with Keithley 6482 2-channel picoammeter ⑨ Ohmite MOX94021006FVE 100 M Ω resistors in series with Applied Kilovolts HP030RIP020 HV.

used high voltage metals are cataloged in Table 2. Our goal is to use the material that sustains the highest electric field strength while minimizing leakage current and magnetic impurities that could introduce EDM systematic effects. Stainless steel was excluded from our testing due to its relatively high ferromagnetic content but its properties are nevertheless included for reference.

Large-grain niobium electrodes with a cathode area of 3170 mm² have been tested to fields as high as 18.7 kV/mm [25]. Fine-grain appears to perform slightly worse, perhaps because the higher grain boundary density increases particulate adherence to the electrode surface [28]. The highest reported electric field for gap sizes near 1 mm that we found is 130 kV/mm using an asymmetric titanium anode and molybdenum cathode with an effective area of 7 mm² [29]. The effective area of the Ra EDM electrode is 200 mm², approximately a factor of thirty larger. There is evidence that larger stressed areas are prone to lower breakdown voltages, suggesting that a miniaturized Ra EDM electrode geometry could improve the maximum stable electric field [30].

In the presence of high electric fields, an oxide layer on an electrode surface could be a significant source of particle emission. Niobium oxidizes at a higher rate than titanium and oxygen-free copper [31, 32, 33, 34, 35]. However, significant oxidation rates for these materials have only been observed at temperatures in excess of 500 $^{\circ}$ C [31, 35, 34, 36, 37]. The Ra EDM experimental apparatus is pumped to ultrahigh vacuum ($< 10^{-11}$ Torr) at room temperature. We therefore expect that oxidation rates are negligibly low for any selection of the considered electrode materials.

We have considered a potential EDM systematic arising

from magnetic impurities in the electrodes that change polarization with each electric field reversal. A sufficiently high concentration of such impurities could perturb the magnetic field in the radium cloud region. To address this, we measured the magnetization of copper, niobium, and titanium electrode-sized pucks in a magnetically shielded mu-metal enclosure with commercial fluxgates (Bartington Mag03IEL70). Titanium was the most magnetic, in agreement with the magnetic properties listed in Table 2. A custom atomic vapor cell magnetometer with a 5 mm cube cell was also used to measure the magnetization of a pair of titanium electrodes to ≤ 5 nT. These measurements informed our choice of large-grain niobium electrodes for the second generation EDM measurements.

2.3. Second generation electrode surface processing

We fabricated four pairs of large-grain niobium electrodes and two pairs of grade-2 titanium electrodes in two separate batches. Surface treatment procedures for each electrode pair are cataloged in Table 3 (batches 2 and 3).

Our target validation field strength was 15 kV/mm or better for this phase of the Ra EDM high voltage development. With this in mind, we used processing procedures informed by discussions with Jefferson Lab accelerator physicists and a review of the literature. All but one of the second generation electrode pairs are chemically polished prior to HPR. Recently, centrifugal barrel polishing has been shown to reduce the required conditioning time compared to chemical etching [38]. This is an encouraging prospect for conditioning Ra EDM electrodes to significantly higher fields in a future phase of development.

The four titanium electrodes (Ti_1 , Ti_2 , Ti_3 , and Ti_4) were mechanically polished with silicon carbide after fabri-

Table 4: Surface decontamination comparison. P = rinse pressure, T = rinse time, CR = clean room, RR = rinse resistivity.

Lab	P (psi)	T (min)	RR (M Ω cm)	CR (Class)	Ref.
CERN	1500	30	18	100	[39]
JLab	1200	20	> 18	-	[25]
KEK	1100	5	80	100	[29]
MSU	1200	20	18.1	100	This work

cation. Their mean surface roughness averages were measured in the range 16–23 nm using a profilometer (MicroXAM) in a clean room. We electropolished pair Ti₁₃ commercially and remeasured the electrode surfaces. We observed an increase in the surface roughness of the electropolished titanium electrodes by $\approx 50\%$ and microprotrusions in the range 1–10 μm .

We decontaminate the electrodes in clean rooms at the Facility for Rare Isotope Beams (FRIB) after polishing. The electrodes are cleaned with detergent and rinsed with pure water in an ultrasonic bath in a staging area. They are rinsed in a second ultrasonic bath with UPW inside a Class 100 clean room. The electrodes are then high pressure-rinsed with UPW at 1200 psi for twenty minutes. After HPR, the electrodes dry in the clean room for several days before being sealed in poly tubing backfilled with dry, filtered nitrogen. A summary of clean room and HPR parameters from several high-gradient development groups is given in Table 4.

3. Electrode Discharge-Conditioning

3.1. High voltage test station

A schematic of the MSU high voltage test station is shown in Figure 6. Electrode pairs are mounted to a polyether ether ketone (PEEK) holder inside a six-way cross vacuum chamber. We estimate current flowing through the PEEK holder (resistivity 10^{16} Ω cm) is limited to less than 6 pA with an electrode voltage of 30 kV. The vacuum chamber is maintained at 10^{-7} Torr with a turbomolecular pump (Pfeiffer Hipace 80). At this pressure the mean free path of residual gas molecules is over a meter, significantly larger than the dimensions of the chamber.

The test station is frequently brought to atmospheric pressure for upgrades and electrode installations. We perform this work in clean rooms that are validated to Class 100 or better with a NIST-calibrated particle counter (Lighthouse Handheld 3016). The chamber is backfilled with dry, high-purity nitrogen through a 0.01 μm gas membrane particle filter (Matheson 6190 Series) while venting the chamber and after clean room operations. During initial evacuation the pump rate is controlled at 1 Torr/s with foreline valves to reduce the risk of disturbing vacuum chamber surfaces.

Table 5: Data acquisition and filtering settings. Used filters are bulleted. notch = band-rejection filter.

setting	Nb ₅₆	Nb ₇₈	Ti ₁₃	Nb ₂₃
sample rate (kHz)	16	16	30	30
samples/point	8192	8192	8192	8192
25–35 Hz notch	•	•		
55–65 Hz notch	•	•		
109–113 Hz notch	•	•		
115–125 Hz notch	•	•		
7.5 kHz low-pass	•	•	•	•

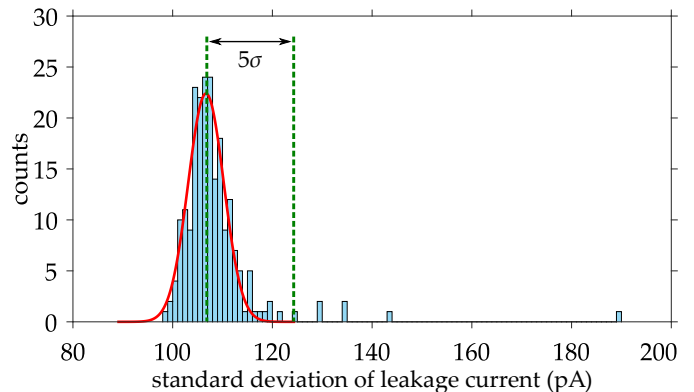


Figure 7: Nb₂₃ at +20 kV/mm over one 60 second cycle during the final hour of conditioning. From the Gaussian fit (solid red line) we determine the mean to be $\bar{x} \pm \sigma = 106.7 \pm 3.6$ pA. There are 207 total data points. We identified 7 events exceeding the $\bar{x} + 5\sigma = 125$ pA threshold as discharges. We typically observe discharge sizes in the range 100–1000 pA, but it is not uncommon to observe larger discharge sizes around 1–10 nA.

We use polished corona ball connections inside and outside the test chamber to minimize discharge risk beyond the electrode gap region. The power supply (Applied Kilovolts HP030RIP020) and feedback resistors are mounted inside a grounded high voltage cage. The feedthroughs are enclosed by grounded “soup can” style shields that can be flooded with dry nitrogen to reduce humidity.

We use a 2-channel picoammeter (Keithley 6482) to measure the current flowing between the electrodes. One channel is not connected and is used to track correlated drifts between the channels. A protection circuit between the electrode and picoammeter suppresses high-power transients that could damage the picoammeter. Typical discharges between the electrodes do not trigger the protection circuit. We calibrated the picoammeter with the protection circuit to within 10 pA.

3.2. Optical measurements of electrodes and gap sizes

Chemical polishing removes thin layers of material from an electrode, minutely reducing its dimensions. We developed an imaging system to measure electrode dimensions and gap sizes without making contact with the electrode. The system uses a CMOS camera and bi-telecentric machine lens (Thorlabs MVTC23024).

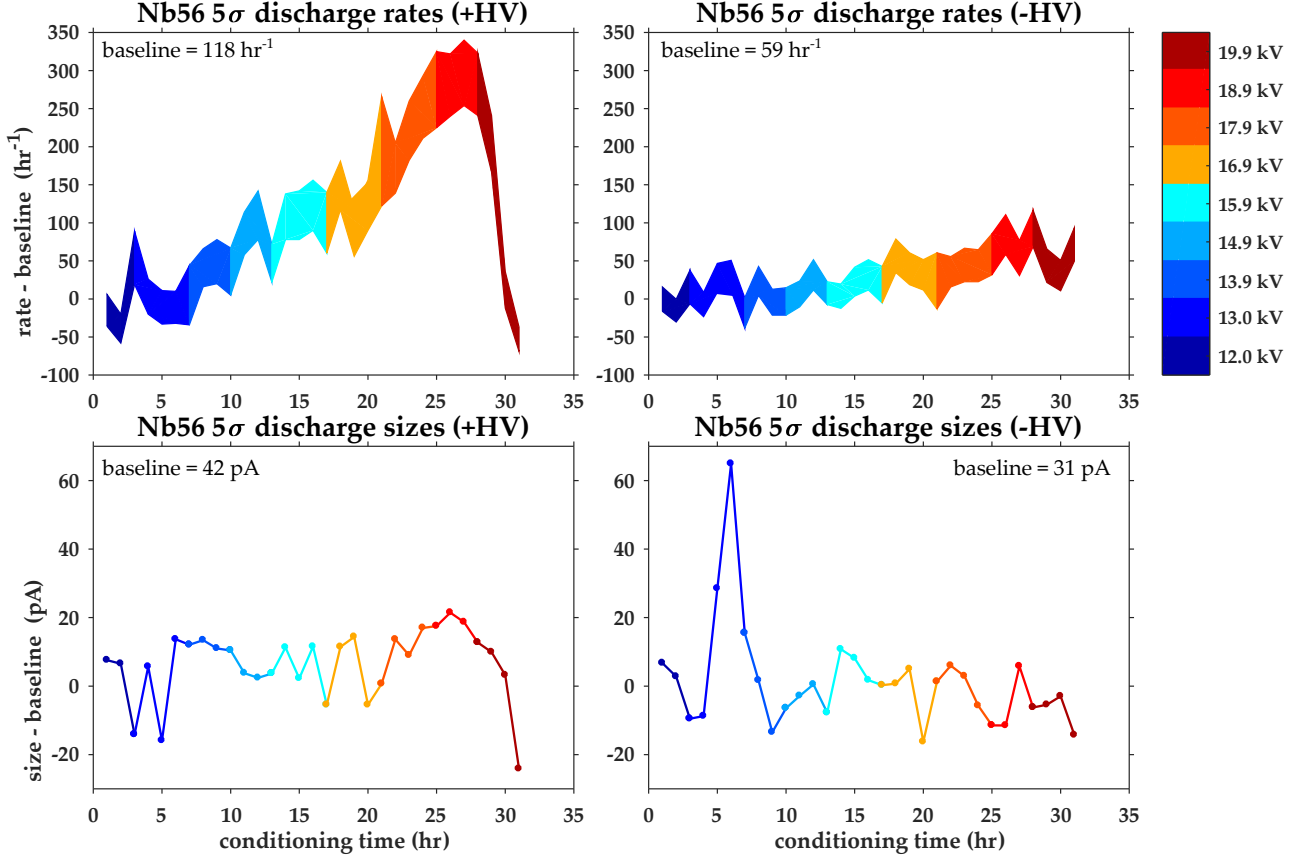


Figure 8: Discharge-conditioning timeline for Nb₅₆ at a 1 mm gap size.

The Ra EDM experiment requires a gap-measuring precision of 0.1 mm or better. To test the electrodes at different gap sizes, we adjust the gap size *in situ* by translating the bottom electrode vertically with a high-precision linear drive (MDC 660002). We initially tested electrode performance over gap sizes ranging 0.4–2.5 mm before removing the linear drive and standardizing the gap size to 1.0 ± 0.1 mm. The EDM measurement features an ODT with a 50 μm waist size and requires a minimum electrode gap size of 1.0 mm to avoid heating the electrode surface.

3.3. Data acquisition and filtering settings

A complete description of acquisition and filtering settings used for each tested pair of electrodes is given in Table 5. We record the power supply current, power supply voltage, vacuum pressure, leakage current, and rough pump foreline pressure with a 16-bit, 250 kS/s data acquisition device (NI DAQ USB-6218) connected to an office model desktop PC. The analog signals are digitally filtered to remove 60 Hz outlet noise and mechanical vibrations from the vacuum pumps. We initially sampled data at 16 kHz but later increased the sample rate to 30 kHz after upgrading the RAM and hard disk of the DAQ PC. The mean and standard deviation for each recorded data point is calculated from 8192 samples. We removed the outlet noise filters after conditioning several pairs of electrodes because they introduced artificial shapes in the

signal waveform. Comparing the leakage current data of electrode pairs with different filtering settings, we found that the digital filters did not significantly affect the distribution of the dataset discussed in Section 3.4. We are sensitive to absolute currents as small as $\sigma \approx 25$ pA with the acquisition settings described in Table 5.

3.4. Identifying electrode discharges

We observe discharges on a timescale of approximately 2 ms. Each sample mean and standard deviation is calculated over an integration period of ≈ 270 ms. The sample mean is well suited for characterizing the relatively slow steady-state leakage current. On the other hand, we find that the sample standard deviation is effective for counting discrete discharges and estimating discharge size.

The standard deviation of the leakage current monitor signal is derived from 8192 samples over a time period. For a 30 kHz sample rate, this corresponds to a total time period of 273 ms. About 220 leakage current standard deviations are collected over the 60 second time period that corresponds to one high voltage magnitude and polarity setting.

The distribution of these 220 leakage current standard deviations is reasonably modeled as a Gaussian distribution. An example of one set of data over a 60 s time period is given in Figure 7. Using the mean and standard deviation of this distribution, we set a threshold that is five

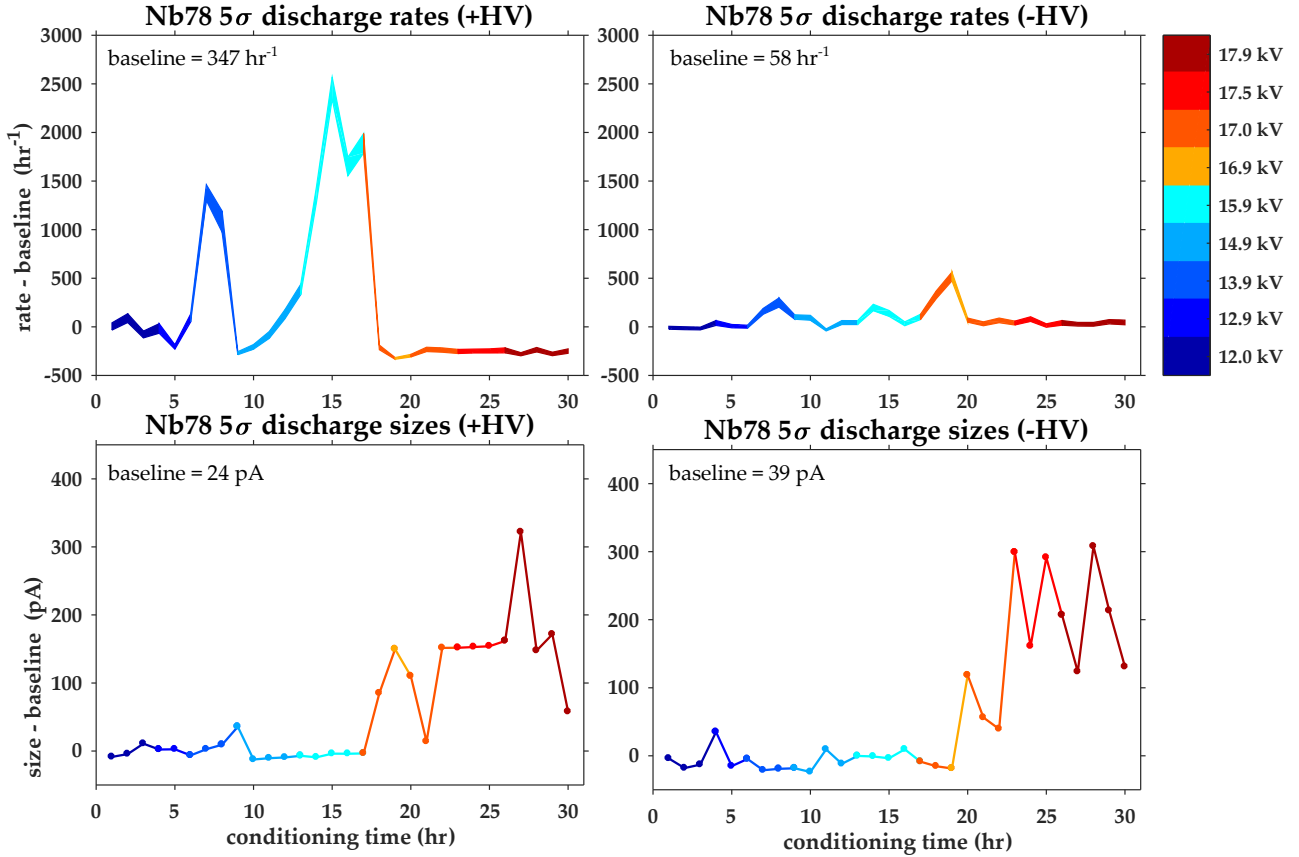


Figure 9: Discharge-conditioning timeline for Nb₇₈ with a 1 mm gap size.

standard deviations above the mean. We define a “discharge” as any leakage current standard deviation above this threshold.

Discharge rates and typical discharge sizes are presented in Figures 8, 9, 10, and 11. A constant “baseline” is subtracted from each plot. We define the baseline as the discharge rate and discharge size at the high voltage magnitude at the start of the conditioning process.

To estimate discharge magnitudes, we report the median value of the standard deviations in each 60 s time period. We expect to see high rates of discharges during discharge-conditioning. Small discharges occurring at a stable rate are beneficial and do not damage the electrode surfaces.

Our discharge counting method does not exclude discharges that could occur at another part of the test station, for example the high voltage feedthroughs. Therefore, we expect our reported discharge rates are conservative overestimates of the true electrode discharge rate.

Additionally, we calculate the steady-state leakage current \bar{I} using the Gaussian mean of each 273 ms time period. \bar{I} is insensitive to discharges, which typically last ≈ 1 ms. For example, in the third hour of conditioning Nb₅₆ at 19.9 kV (see Figure 8), we count a polarity-combined 54 events above the 5σ threshold with the standard deviations but only 2 events with the mean data during the same period.

Our analysis code models the leakage current and cal-

culates the discussed performance metrics. The accuracy of the analysis was independently verified. Code and data availability may be found in Appendix B.

3.5. Discharge-conditioning procedure

Our goal is maximize the electric field strength while minimizing the discharge rate and discharge size. We condition the electrodes at DC voltage, alternating the voltage polarity every 60 s. The voltage is applied to the top electrode. The periodic voltage waveform is chosen to simulate the EDM measurement and is more challenging to stabilize than holding off a static unipolar field. We usually observe the highest rates of discharges during the second and third hours of conditioning.

In the final conditioning phase we validate the electrodes at some fraction of the maximum voltage to reduce the discharge rate. The validation voltage is typically 80–95% of the maximum tested voltage [23, 28].

In Sections 3.6, 3.7, 3.8, and 3.9, we will discuss the discharge-conditioning results of each electrode pair. In Section 3.10, we will compare the overall electrode performance.

3.6. Nb₅₆ conditioning results

The average discharge rate over the course of conditioning the niobium electrode pair Nb₅₆ is shown in the upper panels of Figure 8. At each voltage, the discharge

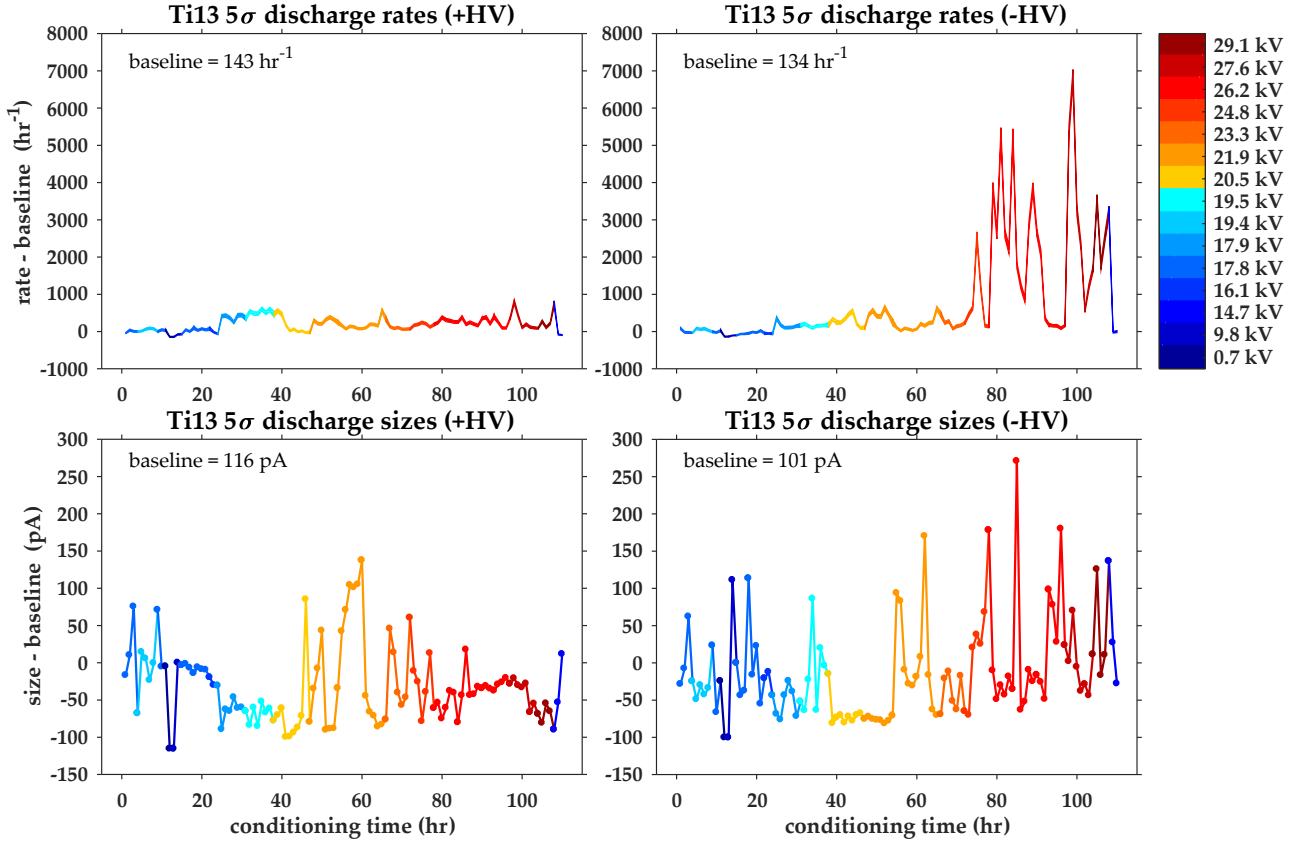


Figure 10: Discharge-conditioning timeline for Ti_{13} at a 0.9 mm gap size.

rates, expressed in discharges per hour (dph), tend to decrease as we condition. There is a step-like increase in discharge rates when the voltage is increased. Nb_{56} was validated at 20 kV / 1 mm with an average discharge rate of 98 ± 19 dph after approximately thirty hours of conditioning.

At negative polarity, the discharge rate increases more slowly with each voltage step. However, the overall curve does not flatten at a minimum count rate as it does at positive polarity. This suggests that additional conditioning could further suppress discharges at negative polarity. It is also possible that the test station design facilitates a higher discharge rate at negative polarity. We will explore this in the near future by conducting conditioning tests while the electrodes are removed from the test station.

Nb_{56} discharge sizes are shown in the lower panels of Figure 8. As we will see with all the discharge plots, the discharge size behavior does not scale with the discharge rate. The largest median discharge size over the course of conditioning is 60 pA, which is relatively small compared to the typical discharge sizes of the other electrode pairs. In the last hour of conditioning the discharge sizes are 20 pA smaller than the starting discharge sizes.

As mentioned in Section 2.1, the legacy copper electrodes were conditioned to 10 kV/mm but could only be operated at 6.5 kV/mm after installing them in the Ra EDM apparatus. For the second generation electrodes,

we made two major improvements to our technique to prevent a similar reduction in field strength. First, our electrodes are now preserved in Class 100 or better clean room environments during conditioning and transport as described in Sections 2.3 and 3.1. Second, we used the new, rigorous discharge-conditioning procedure described Section 3.4 for Nb_{56} and the electrodes discussed in the subsequent sections.

Nb_{56} was installed in the Ra EDM apparatus using the clean room methods described in Section 1.6. They were revalidated at 20 kV/mm after installation. This electrode pair will be used for upcoming second generation EDM measurements.

3.7. Nb_{78} conditioning results

Discharge rates and sizes for the second pair of niobium electrodes Nb_{78} are given in Figure 9. We started conditioning Nb_{78} at 12 kV / 1 mm, the same electric field as Nb_{56} . The initial discharge rates are occasionally in excess of 1000 dph, or about once every three seconds for several hours with discharge sizes of 50 pA. The high discharge rate coupled with low discharge size is an indication that we are operating at an optimized voltage for discharge-conditioning. During the last 10 hours of conditioning the discharge rates decrease to less than the initial rates. The final conditioning shift was performed at 17.8 kV/mm.

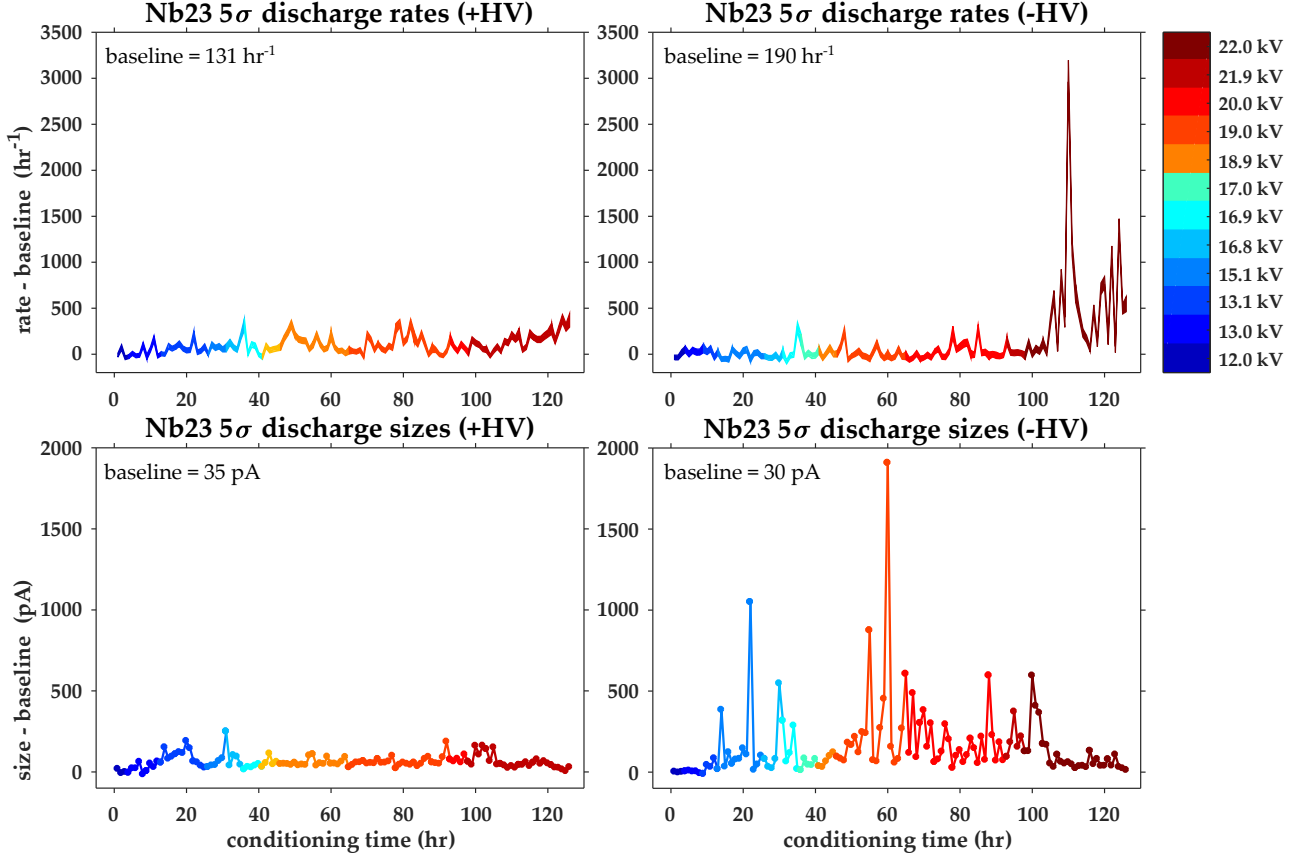


Figure 11: Discharge-conditioning timeline for Nb₂₃ at a 1 mm gap size.

These electrodes were packaged according to our procedure described in Section 1.6 and shipped to the University of Science and Technology of China, where they are being used in an ytterbium EDM measurement.

3.8. Ti₁₃ conditioning results

We changed our data acquisition and digital filter settings for Ti₁₃ and the pair that we will discuss in Section 3.9 (see Table 5). To reach electric fields higher than 20 kV/mm, we conditioned the titanium electrodes for ≈ 110 hours, four times longer than the previous pairs.

Discharge rates and sizes for the titanium electrodes are shown in Figure 10. We started conditioning the electrodes at 14.9 kV / 0.9 mm = 16.5 kV/mm. The initial discharge sizes are approximately 100 pA, significantly higher than Nb₅₆ and Nb₇₈. The discharge rates did not consistently decrease over the course of several shifts at 19.4 kV. At hour 12, we reduced the voltage to 0.7 kV for one shift to verify that the discharge rates decrease before resuming testing at higher voltages.

The discharge rate increases from 290 dph to 5550 dph when stepping the voltage from -26.2 kV to -27.6 kV. This step-like ‘switching on’ of leakage emission sites is consistent with our expectations, given the physical picture of conditioning we describe in Section 1.6. In principle, the emission sites, which may be thought of as microprotrusions, are ablated after spending sufficient time

discharge-conditioning the electrodes. The factors influencing the required amount of time include the smoothness of the high-gradient surfaces, the gap size, and the applied voltage. We were unable to significantly reduce the discharge rates at 27.6 kV / 0.9 mm = 30.7 kV/mm despite more than twenty hours of conditioning.

During the final shift, we reduced the voltage to 14.7 kV / 0.9 mm = 16.3 kV/mm and again observed the discharge rates returning to the baseline. Ti₁₃ can likely be conditioned to perform stably at ≈ 24 kV, or 85% of the maximum applied voltage with additional conditioning. However, the concentration of magnetic impurities in our titanium electrodes (shown in Table 2) is likely too high to be used for an EDM measurement.

3.9. Nb₂₃ conditioning results

We first tested Nb₂₃ at a 0.4 mm gap with fields as high as +52.5 kV/mm and -51.5 kV/mm using the traditional hold-off or ‘current-conditioning’ method [23]. Then we discharge-conditioned the electrodes with the periodic waveform described in Section 3.4 to 27.5 kV/mm. During the subsequent 30 kV/mm conditioning shift, an approximately 100 nA discharge triggered a current avalanche that rapidly increased the leakage current and damaged the electrodes. We were unable to recover meaningful performance with discharge-conditioning and repolished the surface according to Table 3.

Table 6: Electrode conditioning summary. E_i = initial field strength. E_{\max} = max field strength. E_f = final validated field strength. R_i (R_f) = initial (final) discharge rate. \bar{I} = steady-state current at E_f .

pair	E_i (kV/mm)	E_{\max} (kV/mm)	E_f (kV/mm)	$\frac{R_f}{R_i}$	\bar{I} (pA)
Nb ₅₆	11.9	19.8	19.8	1.6	< 10
Nb ₇₈	12.0	17.9	17.9	0.9	< 10
Ti ₁₃	19.8	32.3	29.1	2.2	< 30
Nb ₂₃	12.0	22.0	21.9	1.3	< 25

Repolished Nb₂₃ discharges rates are shown in Figure 11. The rates stay near the baseline, about 200 dph for both polarities up to 20 kV. When we increased the voltage from 20 to 22 kV, the discharge rates become as high as 3000 dph (about once every second). The discharge sizes were low, less than 500 pA, so we continued conditioning at this voltage. Despite conditioning the electrodes at 22 kV/mm for more than twenty hours, the discharge rate remained high. We expect that reducing the voltage by ≈ 1 kV will restore the baseline discharge rate.

As noted previously, we were conditioning Nb₂₃ at 30 kV/mm before a destructive discharge inhibited performance. We recovered 80% of the original electric field performance by repolishing and reconditioning Nb₂₃.

3.10. Comparison of overall electrode performance

Table 6 compares the electric fields tested and discharge rates observed for all of the conditioned electrode pairs averaged over both polarities. E_i is the electric field strength at the start of the conditioning, while E_{\max} is the electric field strength at the end of the conditioning. E_i was chosen, based on the best performance reported in the literature, to be sufficiently low to minimize the possibility of a catastrophic discharge while sufficiently high to minimize the conditioning time. E_f is the final validated field strength, and can be some percent lower than E_{\max} . This is a customary margin which helps ensure stable performance [23, 28].

All the electrodes were discharge-conditioned to higher than our original goal of 15 kV/mm. The steady-state currents \bar{I} at E_f are under the EDM experimental threshold of 100 pA. The ratio of the discharge rate at the final field strength to the initial field strength R_f/R_i are within a factor of 2.2. In the case of Nb₇₈, the final average discharge rate is lower than the initial discharge rate. We conditioned Ti₁₃ most aggressively and it has both the highest final field strength and largest relative increase in discharge rate.

Of particular note is the polarity dependence of the electrode discharge rates. In all cases except for Nb₂₃, the negative polarity discharge rates are significantly higher than the discharge rates at positive polarity. Polarity-dependent discharge rates could be a feature of permanently grounding the bottom electrode and only charging

the top electrode, as illustrated by Figure 6. In the future, we plan to design a more symmetric test station that will alternate the role of grounded and charged electrode to further investigate this effect.

We calculated the steady-state leakage current for all conditioning runs by subtracting the Gaussian means of zero voltage periods from those of high voltage periods. This removes leakage offsets and drifts due to the picoammeter, protection circuit, and power supply. The steady-state leakage current versus voltage trend is modestly linear with an ohmic resistance of 40 kV/10 pA $\approx 10^{16}$ Ω . We observe large leakage currents > 100 pA, correlated with high discharge rates, for Ti₁₃ and Nb₂₃ beyond 22 kV. In the most extreme case, we measured $\bar{I} \approx -670$ pA during conditioning Ti₁₃ at -27.6 kV.

The steady-state leakage current must be less than 100 pA to avoid systematics that could mimic an EDM signal at our current statistical sensitivity. This criterion is similar to metrics used in other electrode development groups [25, 29]. Our steady-state leakage current sensitivity is limited to ≈ 25 pA. At the Nb₅₆ final validated field strength of 20 kV/mm, the measured steady-state leakage current is below this upper limit.

4. Conclusions and outlook

The Ra EDM experiment searches for the atomic electric dipole moment of ²²⁵Ra. During the measurement, the atom spins precess between a pair of identical plane-parallel electrodes that generate a uniform and stable DC electric field that reverses direction every measurement cycle. We used a pair of oxygen-free copper electrodes that operated at ± 6.7 kV/mm and measured an EDM upper limit of 1.4×10^{-23} e cm in the first generation of measurements. For the second generation measurements, we will use a new pair of large-grain niobium electrodes whose systematic effects have been evaluated to the 10^{-26} e cm level.

Two pairs of grade-2 titanium and four pairs of large-grain niobium electrodes were fabricated and polished according to surface preparation techniques that we adapted from accelerator physics literature. We constructed a high voltage test station to condition high voltage electrodes at gap sizes of 0.4–2.5 mm with a 30 kV bipolar power supply at MSU. Procedures were developed to decontaminate electrodes and preserve them in Class 100 environments.

We discharge-conditioned three pairs of niobium electrodes and one pair of titanium electrodes, alternating the polarity of the applied DC field every 60 s to mimic the EDM measurement. Electric fields were tested as high as +52.5 kV/mm and -51.5 kV/mm. All the electrodes exhibited less than 100 pA steady-state leakage current when operated under 22 kV. We validated a pair of large-grain niobium electrodes at 20 kV/mm with an average discharge rate of 98 ± 19 discharges per hour and a steady-state leakage less than 25 pA (1σ).

The large-grain niobium electrodes (Nb₅₆) were transported to ANL and installed in the Ra EDM apparatus all while preserving the electrodes in Class 100 environments. After installation, the performance of Nb₅₆ was revalidated at 20 kV/mm. The improved electric field strength is expected to contribute a factor of 3.1 increase in our EDM statistical sensitivity.

In the next phase of the Ra EDM high voltage development, we will design a more symmetric high voltage test chamber using a unipolar power supply that alternates the field direction by switching connections between the electrodes. Our plan is to discharge-condition electrodes to operate reliably at ± 50 kV/mm across a 1 mm gap.

Acknowledgments

The authors would like to thank: Matthew Poelker and the Electron Gun group at Jefferson Lab for fabricating our electrodes and advising on polishing techniques; TU Munich (TUM) for sharing their mu-metal prototype enclosure for our electrode magnetization measurements; Zheng-Tian Lu and his EDM group at the University of Science and Technology of China for sharing their electrode magnetization measurements; Laura Popielarski and Daniel Victory (FRIB) for helping us high-pressure rinse our electrodes; and Samuel Nash (NSCL) for advising us on clean room design and validation.

We acknowledge support from: Michigan State University; US DOE Office of Science, Office of Physics under DE-AC02-06CH11357; DOE Oak Ridge Institute for Science and Education DE-SC0014664; DOE National Nuclear Security Administration through NNSC DE-NA0003180; and US DOE Office of Science, Office of Nuclear Physics under contract DE-SC0019455.

Appendix A. Magnetic Johnson noise

One source of magnetic field instability that could potentially limit the sensitivity of this experiment is the Johnson-Nyquist noise [40, 41] from conducting materials near the detection region. Thermal agitation (i.e. energy fluctuations) of the charge carriers inside conductors give rise to this electronic noise with a nearly frequency-independent spectral power density of:

$$\frac{dP_n}{d\nu} = 4k_B T \quad (\text{A.1})$$

where k_B is the Boltzmann constant and T is the temperature in Kelvin. A derivation of this equation as well as a discussion of its frequency dependence is given in [42]. By noting that the power dissipated by a conductor is given by $P = I^2 R$, we can rewrite the noise spectrum in terms of the RMS current noise as:

$$\sqrt{I_n^2} = \sqrt{\frac{dI_n^2}{d\nu}(\Delta\nu)} = \sqrt{\frac{4k_B T(\Delta\nu)}{R}} \quad (\text{A.2})$$

where R is the resistance and $\Delta\nu$ is the bandwidth. This current noise generates a magnetic field noise spectrum that, in general, depends on the geometry of and distance from the conductor and the frequency.

In general, it is quite onerous to follow the frequency-dependent prescription of Varpula & Poutanen [43] for arbitrary geometries. However, as pointed out by Lamoreux [44], calculating the noise density at zero frequency always provides a conservative upper limit for the noise density at all frequencies. In this case, called the quasistatic case, we ignore the effect of eddy currents and are able to directly apply the Biot-Savart Law to calculate the magnetic field from a steady state current distribution:

$$d\vec{B}(\vec{r}) = \frac{\mu_0}{4\pi} \left[\frac{I d\vec{\ell} \times (\vec{r} - \vec{u})}{|\vec{r} - \vec{u}|^3} \right] \quad (\text{A.3})$$

where $\vec{B}(\vec{r})$ is the magnetic field at the location \vec{r} , I is the current, and $d\vec{\ell}$ is the line element in the direction of the current at the location \vec{u} . This integral over $d\vec{\ell}$ is assumed to be zero for randomly fluctuating noise currents.

On the other hand, the RMS magnetic field is not expected to be zero and, for example, the y -component can be written as:

$$\begin{aligned} dB_y^2 &= \frac{\mu_0^2}{16\pi^2} \left[\frac{\{I_x d\ell_x (r_z - u_z) - I_z d\ell_z (r_x - u_x)\}^2}{|\vec{r} - \vec{u}|^6} \right] \\ &= \frac{\mu_0^2}{16\pi^2} \left[\frac{I_x^2 (d\ell_x)^2 (r_z - u_z)^2 + I_z^2 (d\ell_z)^2 (r_x - u_x)^2}{|\vec{r} - \vec{u}|^6} \right] \end{aligned} \quad (\text{A.4})$$

where I_q is the current in the q direction and the subscripts $q = x, y, z$ label the component of the vectors such that $\hat{x} \times \hat{y} = \hat{z}$.

The randomly fluctuating noise currents in two different directions are assumed to be completely uncorrelated. Therefore, the cross term (i.e. $I_x I_z$) is assumed to integrate to zero and only the quadratic terms (i.e. I_x^2, I_z^2) survive. The field noise density can be written in terms of the current noise density, which, in the q direction, is given by:

$$\frac{dI_{n,q}^2}{d\nu} = \frac{4k_B T}{R_q} = \frac{4k_B T}{\rho} \left(\frac{dA_q}{d\ell_q} \right) \quad (\text{A.5})$$

where R_q is the resistance in the q direction, $d\ell_q$ is the length in the q direction, and dA_q is the cross sectional area normal to the q direction. For example, for a randomly fluctuating current in the x -direction, we have:

$$\frac{dI_{n,x}^2}{d\nu} = \frac{4k_B T}{R_x} = \frac{4k_B T}{\rho} \left(\frac{dA_x}{d\ell_x} \right) = \frac{4k_B T}{\rho} \left(\frac{d\ell_z d\ell_y}{d\ell_x} \right) \quad (\text{A.6})$$

Plugging this into Eqn. (A.4) and dropping the cross terms (as argued before), we find that the q component of the

field noise density is given by:

$$\frac{dB_{n,q}^2}{d\nu} = \left(\frac{\mu_0^2 k_B T}{4\pi^2 \rho} \right) \int \left| \frac{(\vec{r} - \vec{u}) \times \hat{q}}{|\vec{r} - \vec{u}|^3} \right|^2 d^3u \quad (\text{A.7})$$

where $d^3u = (dl_x)(dl_y)(dl_z)$ and the scale factor is

$$\frac{\mu_0^2 k_B T}{4\pi^2 \rho} = \left[\frac{0.989 \text{ pT}}{\sqrt{\text{Hz}}} \right]^2 \left[\frac{T}{273 \text{ K}} \right] \left[\frac{\rho_{\text{Cu}}(273 \text{ K})}{\rho(T)} \right] \cdot \text{cm} \quad (\text{A.8})$$

where $\rho_{\text{Cu}}(273 \text{ K}) = 1.542 \times 10^{-8} \Omega \cdot \text{m}$.

For an infinite conducting plane of thickness d , Varpula & Poutanen [43] have found an analytic form for the noise volume integral:

$$\int \left| \frac{(\vec{r} - \vec{u}) \times \hat{y}}{|\vec{r} - \vec{u}|^3} \right|^2 d^3u = \frac{\pi}{2y} \left[\frac{d}{d+y} \right] \quad (\text{A.9})$$

where y is the distance from the surface of the conducting plane. While a numerical integration of the noise volume integral for the noise in the y -direction converges to the analytic formula above, the same numerical integration suggests that, contrary to the conclusion of Varpula & Poutanen, the three components of the magnetic field noise due to an infinite plane are related by:

$$\left(\frac{dB_{n,x}^2}{d\nu} \right) = \left(\frac{dB_{n,z}^2}{d\nu} \right) = \frac{3}{2} \left(\frac{dB_{n,y}^2}{d\nu} \right) \quad (\text{A.10})$$

Finally, we model the two Ra EDM HV electrodes as cylinders with radius of 1.2 cm and height of 1.6 cm. Assuming a gap between electrodes of 1 mm, noise volume integrals at a location directly in between the electrodes are:

$$\begin{aligned} \int \left| \frac{(\vec{r} - \vec{u}) \times \hat{x}}{|\vec{r} - \vec{u}|^3} \right|^2 d^3u &= \int \left| \frac{(\vec{r} - \vec{u}) \times \hat{z}}{|\vec{r} - \vec{u}|^3} \right|^2 d^3u \\ &= 92.5 \text{ cm}^{-1} \\ \int \left| \frac{(\vec{r} - \vec{u}) \times \hat{y}}{|\vec{r} - \vec{u}|^3} \right|^2 d^3u &= 56.8 \text{ cm}^{-1} \end{aligned} \quad (\text{A.11})$$

For Niobium electrodes ($\rho_{\text{Nb}}/\rho_{\text{Cu}} = 9.85$) that are held at room temperature ($T = 298 \text{ K}$), we calculate a magnetic field noise density of:

$$\begin{aligned} \sqrt{\frac{dB_{n,x}^2}{d\nu}} &= \sqrt{\frac{dB_{n,z}^2}{d\nu}} = 3.17 \frac{\text{pT}}{\sqrt{\text{Hz}}} \\ \sqrt{\frac{dB_{n,y}^2}{d\nu}} &= 2.48 \frac{\text{pT}}{\sqrt{\text{Hz}}} \end{aligned} \quad (\text{A.12})$$

Appendix B. Code and data availability

The code used to analyze the high voltage data and generate the current discharge plots is available for use at <https://zenodo.org/badge/latestdoi/294766922>. The data used for the high voltage analysis may be made available for reasonable requests sent to singhj@frib.msu.edu.

References

- [1] T. E. Chupp, P. Fierlinger, M. J. Ramsey-Musolf, J. T. Singh, [Electric dipole moments of atoms, molecules, nuclei, and particles](#), Rev. Mod. Phys. 91 (2019) 015001. doi:10.1103/RevModPhys.91.015001. URL <https://link.aps.org/doi/10.1103/RevModPhys.91.015001>
- [2] P. Huet, E. Sather, [Electroweak baryogenesis and standard model cp violation](#), Phys. Rev. D 51 (1995) 379–394. doi:10.1103/PhysRevD.51.379. URL <https://link.aps.org/doi/10.1103/PhysRevD.51.379>
- [3] W. C. Haxton, E. M. Henley, [Enhanced \$t\$ -nonconserving nuclear moments](#), Phys. Rev. Lett. 51 (1983) 1937–1940. doi:10.1103/PhysRevLett.51.1937. URL <https://link.aps.org/doi/10.1103/PhysRevLett.51.1937>
- [4] N. Auerbach, V. V. Flambaum, V. Spevak, [Collective \$t\$ - and \$p\$ -odd electromagnetic moments in nuclei with octupole deformations](#), Phys. Rev. Lett. 76 (1996) 4316–4319. doi:10.1103/PhysRevLett.76.4316. URL <https://link.aps.org/doi/10.1103/PhysRevLett.76.4316>
- [5] J. Dobaczewski, J. Engel, [Nuclear time-reversal violation and the schiff moment of \$^{225}\text{Ra}\$](#) , Phys. Rev. Lett. 94 (2005) 232502. doi:10.1103/PhysRevLett.94.232502. URL <https://link.aps.org/doi/10.1103/PhysRevLett.94.232502>
- [6] S. Ban, J. Dobaczewski, J. Engel, A. Shukla, [Fully self-consistent calculations of nuclear schiff moments](#), Phys. Rev. C 82 (2010) 015501. doi:10.1103/PhysRevC.82.015501. URL <https://link.aps.org/doi/10.1103/PhysRevC.82.015501>
- [7] V. A. Dzuba, V. V. Flambaum, J. S. M. Ginges, M. G. Kozlov, [Electric dipole moments of hg, xe, rn, ra, pu, and tlf induced by the nuclear schiff moment and limits on time-reversal violating interactions](#), Phys. Rev. A 66 (2002) 012111. doi:10.1103/PhysRevA.66.012111. URL <https://link.aps.org/doi/10.1103/PhysRevA.66.012111>
- [8] R. H. Parker, M. R. Dietrich, M. R. Kalita, N. D. Lemke, K. G. Bailey, M. Bishof, J. P. Greene, R. J. Holt, W. Korsch, Z.-T. Lu, P. Mueller, T. P. O’Connor, J. T. Singh, [First measurement of the atomic electric dipole moment of \$^{225}\text{Ra}\$](#) , Phys. Rev. Lett. 114 (2015) 233002. doi:10.1103/PhysRevLett.114.233002. URL <https://link.aps.org/doi/10.1103/PhysRevLett.114.233002>
- [9] M. Bishof, R. H. Parker, K. G. Bailey, J. P. Greene, R. J. Holt, M. R. Kalita, W. Korsch, N. D. Lemke, Z.-T. Lu, P. Mueller, T. P. O’Connor, J. T. Singh, M. R. Dietrich, [Improved limit on the \$^{225}\text{Ra}\$ electric dipole moment](#), Phys. Rev. C 94 (2016) 025501. doi:10.1103/PhysRevC.94.025501. URL <https://link.aps.org/doi/10.1103/PhysRevC.94.025501>
- [10] T. Chupp, M. Ramsey-Musolf, [Electric dipole moments: A global analysis](#), Phys. Rev. C 91 (2015) 035502. doi:10.1103/PhysRevC.91.035502. URL <https://link.aps.org/doi/10.1103/PhysRevC.91.035502>
- [11] E. Arnold, W. Borchers, M. Carre, H. T. Duong, P. Juncar, J. Lerme, S. Liberman, W. Neu, R. Neugart, E. W. Otten, M. Pellarin, J. Pinard, G. Ulm, J. L. Vialle, K. Wendt, [Direct measurement of nuclear magnetic moments of radium isotopes](#), Phys. Rev. Lett. 59 (1987) 771–774. doi:10.1103/PhysRevLett.59.771. URL <https://link.aps.org/doi/10.1103/PhysRevLett.59.771>
- [12] M. V. Romalis, E. N. Fortson, [Zeeman frequency shifts in an optical dipole trap used to search for an electric-dipole moment](#), Phys. Rev. A 59 (1999) 4547–4558. doi:10.1103/PhysRevA.59.4547. URL <https://link.aps.org/doi/10.1103/PhysRevA.59.4547>

- [13] M. R. Dietrich, K. G. Bailey, T. P. O'Connor, **Alignment of a vector magnetometer to an optical prism**, Review of Scientific Instruments 88 (5) (2017) 055105. doi:[10.1063/1.4983146](https://doi.org/10.1063/1.4983146). URL <https://doi.org/10.1063/1.4983146>
- [14] H. B. Michaelson, **The work function of the elements and its periodicity**, Journal of Applied Physics 48 (11) (1977) 4729–4733. doi:[10.1063/1.323539](https://doi.org/10.1063/1.323539). URL <http://dx.doi.org/10.1063/1.323539>
- [15] R. G. Wilson, **Vacuum thermionic work functions of polycrystalline be, ti, cr, fe, ni, cu, pt, and type 304 stainless steel**, Journal of Applied Physics 37 (6) (1966) 2261–2267. doi:[10.1063/1.1708797](https://doi.org/10.1063/1.1708797). URL <http://dx.doi.org/10.1063/1.1708797>
- [16] W. Haynes, Handbook of Chemistry and Physics, Taylor & Francis Group, LLC, Boca Raton, Florida, 2014.
- [17] J. Davis, Metals Handbook , ASM International, Materials Park, OH, 1998.
- [18] J. R. Rumble, CRC Handbook of Chemistry and Physics, 101st Edition (Internet Version 2020), Taylor & Francis Group, LLC, Boca Raton, Florida, 2020.
- [19] D. Furrer, S. Semiatin, ASM International, 2010. [link]. URL <https://app.knovel.com/hotlink/toc/id:kpASMHVB03/asm-handbook-volume-22b/asm-handbook-volume-22b>
- [20] G. V. Samsonov, Handbook of the Physicochemical Properties of the Elements, Plenum Publishing Corporation., New York, New York, 1968.
- [21] J. F. O'Hanlon, A User's Guide to Vacuum Technology, John Wiley & Sons, Inc., Hoboken, New jersey, 2003.
- [22] W. T. Diamond, **New perspectives in vacuum high voltage insulation. ii. gas desorption**, Journal of Vacuum Science & Technology A: Vacuum, Surfaces, and Films 16 (2) (1998) 720–735. doi:[10.1116/1.581052](https://doi.org/10.1116/1.581052). URL <http://dx.doi.org/10.1116/1.581052>
- [23] R. Latham, High Voltage Vacuum Insulation, Academic Press Inc., San Diego, California, USA, 1995.
- [24] B. Bonin, **Field emission and surface conditioning**, Vacuum 46 (8) (1995) 907 – 912. doi:[http://dx.doi.org/10.1016/0042-207X\(95\)00069-0](http://dx.doi.org/10.1016/0042-207X(95)00069-0). URL <http://www.sciencedirect.com/science/article/pii/S0042207X95000690>
- [25] M. BastaniNejad, M. A. Mohamed, A. A. Elmustafa, P. Adderley, J. Clark, S. Covert, J. Hansknecht, C. Hernandez-Garcia, M. Poelker, R. Mammei, K. Surles-Law, P. Williams, **Evaluation of niobium as candidate electrode material for dc high voltage photoelectron guns**, Phys. Rev. ST Accel. Beams 15 (2012) 083502. doi:[10.1103/PhysRevSTAB.15.083502](https://doi.org/10.1103/PhysRevSTAB.15.083502). URL <https://link.aps.org/doi/10.1103/PhysRevSTAB.15.083502>
- [26] B. Graner, Electric and magnetic field preparation for measurement of the 225ra permanent electric dipole moment (2009).
- [27] R. Parker, First EDM measurement of radium, Ph.D. thesis, The University of Chicago (Jan 2015).
- [28] R. Latham, High Voltage Vacuum Insulation: A New Perspective, AuthorHouse, Bloomington, Indiana, USA, 2006.
- [29] F. Furuta, T. Nakanishi, S. Okumi, T. Gotou, M. Yamamoto, M. Miyamoto, M. Kuwahara, N. Yamamoto, K. Naniwa, K. Yasui, H. Matsumoto, M. Yoshioka, K. Togawa, **Reduction of field emission dark current for high-field gradient electron gun by using a molybdenum cathode and titanium anode**, Nuclear Instruments and Methods in Physics Research Section A: Accelerators, Spectrometers, Detectors and Associated Equipment 538 (1) (2005) 33 – 44. doi:<http://dx.doi.org/10.1016/j.nima.2004.08.131>. URL <http://www.sciencedirect.com/science/article/pii/S0168900204020170>
- [30] N. S. Phan, W. Wei, B. Beaumont, N. Bouman, S. M. Clayton, S. A. Currie, T. M. Ito, J. C. Ramsey, G. M. Seidel, A study of dc electrical breakdown in liquid helium through analysis of the empirical breakdown field distributions (2020). arXiv: [2011.08844](https://arxiv.org/abs/2011.08844).
- [31] J. Sheasby, **The Oxidation of Niobium in the Temperature Range 450-720 C**, Journal of the Electrochemical Society 115 (1968) 695. doi:<https://doi.org/10.1149/1.2411404>. URL <http://jes.ecsdl.org/content/115/7/695.short>
- [32] B. Argent, B. Phelps, **The oxidation of niobium-titanium and niobium-molybdenum alloys**, Journal of the Less Common Metals 2 (2) (1960) 181 – 190, conference on Niobium, Tantalum, Molybdenum and Tungsten. doi:[https://doi.org/10.1016/0022-5088\(60\)90013-8](https://doi.org/10.1016/0022-5088(60)90013-8). URL <http://www.sciencedirect.com/science/article/pii/S0022508860900138>
- [33] P. Kofstad, P. Anderson, O. Krudtaa, **Oxidation of titanium in the temperature range 800–1200 c**, Journal of the Less Common Metals 3 (2) (1961) 89 – 97. doi:[https://doi.org/10.1016/0022-5088\(61\)90001-7](https://doi.org/10.1016/0022-5088(61)90001-7). URL <http://www.sciencedirect.com/science/article/pii/S0022508861900017>
- [34] E. Gemelli, N. Camargo, **Oxidation kinetics of commercially pure titanium**, Materia (Rio de Janeiro) 12 (2007) 525 – 531. doi:[10.1590/S1517-70762007000300014](https://doi.org/10.1590/S1517-70762007000300014). URL https://www.scielo.br/scielo.php?pid=S1517-70762007000300014&script=sci_arttext&tlng=pt
- [35] L. Ogbuji, D. Humphrey, **Comparison of the oxidation rates of some new copper alloys**, Oxidation of Metals 60 (3) (2003) 271–291. doi:[10.1023/A:1026019202691](https://doi.org/10.1023/A:1026019202691). URL <https://doi.org/10.1023/A:1026019202691>
- [36] M. Sun, X. Wu, Z. Zhang, E.-H. Han, **Oxidation of 316 stainless steel in supercritical water**, Corrosion Science 51 (5) (2009) 1069 – 1072. doi:<https://doi.org/10.1016/j.corsci.2009.03.008>. URL <http://www.sciencedirect.com/science/article/pii/S0010938X09000985>
- [37] E. Gulbransen, K. Andrew, F. Brassart, **Oxidation of Molybdenum 550 to 1700 C**, Journal of the Electrochemical Society 110 (1963) 952 – 959. doi:<https://doi.org/10.1149/1.2425918>. URL <http://jes.ecsdl.org/content/110/9/952.short>
- [38] C. Hernandez-Garcia, D. Bullard, F. Hannon, Y. Wang, M. Poelker, **High voltage performance of a dc photoemission electron gun with centrifugal barrel-polished electrodes**, Review of Scientific Instruments 88 (9) (2017) 093303. doi:[10.1063/1.4994794](https://doi.org/10.1063/1.4994794). URL <https://doi.org/10.1063/1.4994794>
- [39] P. Bernard, D. Bloess, W. Hartung, C. Hauviller, W. Weingarten, P. Bosland, J. Martignac, **Superconducting niobium sputter coated copper cavities at 1500-MHz**, Part. Accel. 40 (1992) 487–496.
- [40] J. B. Johnson, **Thermal agitation of electricity in conductors**, Phys. Rev. 32 (1) (1928) 97. doi:[10.1103/PhysRev.32.97](https://doi.org/10.1103/PhysRev.32.97).
- [41] H. Nyquist, **Thermal agitation of electric charge in conductors**, Phys. Rev. 32 (1) (1928) 110–113. doi:[10.1103/PhysRev.32.110](https://doi.org/10.1103/PhysRev.32.110).
- [42] D. Abbott, B. Davis, N. Phillips, K. Eshraghian, **Simple derivation of the thermal noise formula using window-limited fourier transforms and other conundrums**, Education, IEEE Transactions on 39 (1) (1996) 1 –13. doi:[10.1109/13.485226](https://doi.org/10.1109/13.485226).
- [43] T. Varpula, T. Poutanen, **Magnetic field fluctuations arising from thermal motion of electric charge in conductors**, Journal of Applied Physics 55 (11) (1984) 4015–4021. doi:[10.1063/1.332990](https://doi.org/10.1063/1.332990). URL <https://aip.scitation.org/doi/10.1063/1.332990>
- [44] S. K. Lamoreaux, **Feeble magnetic fields generated by thermal charge fluctuations in extended metallic conductors: Implications for electric-dipole moment experiments**, Phys. Rev. A 60 (2) (1999) 1717–1720. doi:[10.1103/PhysRevA.60.1717](https://doi.org/10.1103/PhysRevA.60.1717).